Available online at www.sciencedirect.com
ScienceDirect
International Journal of Heat and Mass Transfer 51 (2008) 553–565
International Journal of HEAT and MASS TRANSFER
www.elsevier.com/locate/ijhmt

Numerical predictions for stable buoyant regimes within a square cavity containing a heated horizontal cylinder

Diego Angeli, Paolo Levoni, Giovanni S. Barozzi *

Dipartimento di Ingegneria Meccanica e Civile, Università di Modena e Reggio Emilia, Via Vignolese, 905 141100 Modena, Italy

Received 6 April 2006
Available online 6 August 2007

Abstract

Buoyancy-induced flow regimes are investigated numerically for the basic case of a horizontal cylinder centred into a long co-axial square-sectioned cavity. In the frame of the 2D assumption, the threshold for the occurrence of time-dependent behaviour is explored. Stable symmetric and non-symmetric steady-state solutions, as well as unsteady regimes are observed, depending on the Rayleigh number, *Ra*, and the aspect ratio of the cavity, *d*. Four *d*-values are considered ($d = 0.2$, 0.4, 0.6, and 0.8). Heat transfer results are correlated by a single equation covering the full subcritical region.

Keywords: Natural convection; Enclosures; Flow stability; DNS; Heat transfer correlation

1. Introduction and scope

Buoyancy-induced flows play a central role in a number of practical applications, including environmental thermal control, nuclear design, solar heating, and the cooling of electronic devices. More generally, almost all technologies involving passive heat transfer as the main source of thermal dissipation rely upon natural convection effects.

Natural convection from isolated sources has been investigated for years, and heat transfer correlations for most basic geometries can be retrieved from heat transfer handbooks [1–3]. Natural convection in enclosures has also been the subject of intensive research efforts, and its fundamentals are now summarized in monographs and review works [4–7]. In such a context, major problems are the prediction of the flow regimes and patterns, and the effect of confinement on heat transfer performances. This, in turn, implies the reliability of heat transfer correlations as derived for isolated sources.

In this paper, 2D numerical predictions are presented for the case of a circular source centred into a square cavity. The isolated horizontal cylinder constitutes the basic reference for the geometry under consideration. That fundamental case is well established in the literature, starting from McAdams' pioneering work [8], up to the most complete heat transfer correlations by Churchill and Chu [9] and Morgan [10], covering both laminar and turbulent regimes and valid for all Prandtl numbers.

The thermal interaction between a cylindrical source and a rectangular enclosure was first investigated by Ghaddar [11]: a uniformly heated 2D circular source in a rectangular cavity was considered numerically, using a spectral element method. Flow patterns and heat transfer rates were predicted for air over a wide range of *Ra*-values. The case of an isothermal cylinder in a rectangular cavity was investigated by Cesini et al. [12] by both experiments and numerical modelling. Results were presented in terms of the local and averaged Nusselt numbers, for different values of the cavity aspect ratio.

The work of Moukalled and Acharya [13] is of primary concern here, since they were the first to bring forth a numerical analysis of the convective annulus created by

* Corresponding author. Tel.: +39 059 2056148; fax: +39 059 2056126.
E-mail address: barozzi.giovanni@unimore.it (G.S. Barozzi).

0017-9310/$ - see front matter © 2007 Elsevier Ltd. All rights reserved.
doi:10.1016/j.ijheatmasstransfer.2007.05.007

Nomenclature

a, b	constants in Eq. (27)
d	cylinder diameter to cavity side ratio
D	diameter of the cylindrical source
g	modulus of the gravitational acceleration
$\hat{\mathbf{g}}$	gravity unit vector
h	dimensionless gap width
h_θ	local heat transfer coefficient
h_{av}	average heat transfer coefficient
H	gap width
L	cavity side length
n	exponent in Eq. (23)
Nu	Nusselt number
p	pressure
P	scale pressure
Pr	Prandtl number
r	radial coordinate
Ra	Rayleigh number
t	time
T	temperature
$\mathbf{u}$	velocity vector
U	scale velocity
x, y, z	Cartesian coordinates
Y, Z	dependent and independent variables in Eq. (23)

Greek symbols

α	thermal diffusivity
β	thermal expansion coefficient
ε	relative error
θ	angular coordinate
λ	thermal conductivity
ν	kinematic viscosity
ξ	grid spacing
ρ	density
τ	reference time
φ	non-dimensional wall heat flux
Φ	oscillation amplitude of the non-dimensional wall heat flux
ω	non-dimensional frequency

Subscripts

0	pseudo-diffusive
av	average
D	diameter
E	enclosure
H	gap width
L	cavity side
S	source
θ	local

Superscripts

*	non-dimensional variable
$^-$	time-averaged quantity

an inner circular cylinder and an outer square cylinder. Numerical simulations were performed for three values of the ratio between the cylinder radius and the cavity side, the aspect ratio, and five values of the Rayleigh number. The finite-volume method adopted involved the use of structured boundary-fitted curvilinear meshes, to solve the momentum and energy equations in their steady-state formulation. Flow patterns and thermal fields in all configurations were presented, alongside with profiles of the local Nusselt number on both the enclosure walls and the cylinder surface. An asymptotic correlation for the averaged Nusselt number was proposed, including the effect of both parameters. Results in [13] were recently used by Shu and Zhu [14], and by Peng et al. [15] for the sake of validation of their numerical procedures. In the former case a numerical approach based on the differential quadrature method was used. The technique allowed accurate solutions to be obtained while adopting relatively coarse grids. Peng et al. [15] employed a Lattice Boltzmann method, and estimated its accuracy and suitability to the simulation of buoyancy-driven flows. The addition of fresh quantitative data was scarce in that case.

Steady-state formulations were always adopted in the above numerical experiments. However, it is well documented that, above some critical values of the Rayleigh number, confined buoyant flows may undergo different types of bifurcations, giving rise to unsteady flow regimes having deterministic or chaotic features. An interesting study upon time-dependent buoyant flow induced by an enclosed thermal source was carried out numerically by Desrayaud and Lauriat [16]. They investigated very thoroughly the dynamical behaviour of the buoyant plume arising from a horizontal line source in a rectangular cavity. Deschamps and Desrayaud [17] highlighted the substantial concordance between results for wires of small diameter and line heat sources [16]. The issue was later addressed by Corticelli and Barozzi [18], who also considered the cases of an enclosed rectangular source and an encapsulated vertical channel [19,20].

In the light of the above literature, it is pointed out here that the detection of the transition threshold from steady-state to time-dependent regimes not only is of basic scientific interest, but also has practical significance. The character of the flow regime, in turn, is expected to affect heat transfer, even if the extent of such an influence remains unpredictable for the time being.

In the present work, the basic case already considered in [13–15] is revisited and extended according to the following lines:

(i) the limits of the long-term steady-flow regimes are explored using direct numerical simulation for four values of the aspect ratio;
(ii) the CFD software FLUENT 6.2 is employed for steady-state flow-field and heat transfer predictions;
(iii) results for the averaged Nusselt number are abridged in a unique heat transfer correlation for air, covering the whole subcritical range of the Rayleigh number, and including the effect of the ratio between the source diameter and the cavity side.

2. Physical model

The case to be considered is shown in Fig. 1. A horizontal cylinder of diameter D is centred into a cavity of square cross section. The y-axis of the coordinate system coincides with the cylinders longitudinal axis, while the z-axis is parallel and opposed to the gravitational field. The cavity extension along y is assumed to prevail over L, the cavity side length, so that the flow and temperature fields can be modelled as two-dimensional. The wall temperature of the cylindrical source is uniform, $T = T_S$; the enclosure walls are also isothermal, $T = T_E$, with $T_S > T_E$. The working fluid is assumed to be air.

The problem is stated in terms of the incompressible Navier–Stokes formulation. The Oberbeck–Boussinesq approximation is enforced [21]. All the fluid properties are consistently assumed to be constant, apart from density in the buoyancy term of the z-momentum equation.

The continuity, momentum, and energy equations are given the following non-dimensional form, where the non-dimensional variables appear as starred:

$$\nabla \cdot \mathbf{u}^* = 0, \tag{1}$$

$$\frac{\partial}{\partial t}\mathbf{u}^* + \mathbf{u}^* \cdot \nabla \mathbf{u}^* = -\nabla p^* + \frac{1}{\sqrt{Gr}}\nabla^2 \mathbf{u}^* + T^* \hat{\mathbf{g}}, \tag{2}$$

$$\frac{\partial T^*}{\partial t^*} + \mathbf{u}^* \cdot \nabla T^* = \frac{1}{\sqrt{GrPr}}\nabla^2 T^*. \tag{3}$$

The buoyancy force in Eq. (2) is associated to the gravitational unit vector, $\hat{\mathbf{g}}$, and no source term is included in the energy equation (3).

The cylinder diameter, D, is used as the scale length. The scale velocity, U, the leading temperature difference, the time scale and the reference pressure are respectively defined:

$$U = (g\beta D \Delta T)^{1/2}, \tag{4}$$

$$\Delta T = T_S - T_E, \tag{5}$$

$$\tau = \frac{D}{U}, \tag{6}$$

$$P = \rho U^2, \tag{7}$$

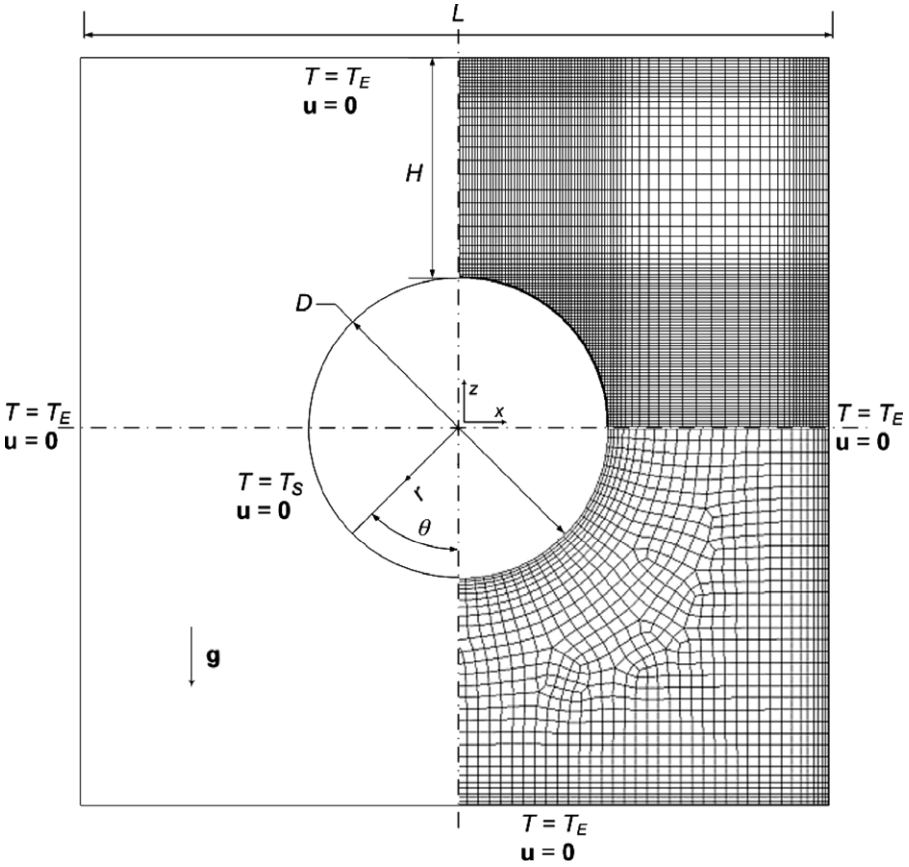

Fig. 1. Schematic of the problem for $d = 0.4$; detail of the 166×166 grid for DNS (upper right quarter); detail of the grid (2514 elements) for steady-state predictions (lower right quarter).

ρ being the reference density for the Oberbeck–Boussinesq extrapolation.

The boundary conditions at the source and the enclosure walls respectively are:

$$T^* = 1, \quad \mathbf{u}^* = 0, \tag{8}$$

$$T^* = 0, \quad \mathbf{u}^* = 0. \tag{9}$$

The Prandtl number, Pr, the Grashof number, Gr_D, and the Rayleigh number, Ra_D, are respectively defined:

$$Pr = \frac{\nu}{\alpha}, \tag{10}$$

$$Gr_D = \left(\frac{UD}{\nu}\right)^2, \tag{11}$$

$$Ra_D = Gr_D \cdot Pr. \tag{12}$$

Under the assumption of constant-property fluid, the Prandtl number is set as $Pr = 0.7$.

The cavity side, L, and the minimum gap between the cylinder and the enclosure walls, H, are alternative scale lengths for the system under consideration. These are related:

$$H = \frac{L - D}{2}. \tag{13}$$

The aspect ratio of the system is defined:

$$d = \frac{D}{L}. \tag{14}$$

The gap width to diameter ratio can also be used:

$$h = \frac{H}{D} = \frac{1 - d}{2d}. \tag{15}$$

The local Nusselt number on the cylinder surface, is defined:

$$Nu_{D,\theta} = \frac{h_\theta D}{\lambda} = -\left(\frac{\partial T^*(\theta)}{\partial r^*}\right)_{r^*=\frac{1}{2}}. \tag{16}$$

Here, h_θ designates the local heat transfer coefficient, being θ the angular coordinate in Fig. 1. The average Nusselt number on the cylinder surface is defined as:

$$Nu_D = \frac{h_{\mathrm{av}} D}{\lambda} = \frac{1}{2\pi}\int_0^{2\pi} Nu_{D,\theta}\,\mathrm{d}\theta. \tag{17}$$

Alternative definitions of the Rayleigh and Nusselt numbers are based on L or H. These are related to Ra_D, and Nu_D as follows:

$$Ra_L = Ra_D/d^3, \tag{18}$$

$$Ra_H = Ra_D \cdot h^3, \tag{19}$$

$$Nu_L = Nu_D/d, \tag{20}$$

$$Nu_H = Nu_D \cdot h. \tag{21}$$

3. Numerical methods

Two alternative numerical approaches were adopted in the simulations, both based on control volume discretizations of Eqs. (1)–(3).

A direct numerical simulation (DNS) technique was used in the first part of the investigation, to explore the asymptotic behaviour of the system over a wide range of Ra-values. The DNS method is based on a finite volume implementation of a second order projection method, following Gresho [22]. Time-discretizations of the conservation equations are performed according to a three-level scheme, which is fully implicit for the diffusive terms, and explicit Adams–Bashforth for the advective terms. Such a practice is second-order accurate in time. Besides, the choice of an implicit scheme for the diffusive terms allows to remove the stability constraint on the time-step width. Spatial derivatives are approximated with second order central differences on staggered, non-uniform Cartesian grids. The resolution of the discrete momentum and energy equations at each time-step is made by *approximate factorization*, while the Poisson problem associated with the pressure–velocity coupling [22], is solved through a fast direct Poisson solver, based on *matrix decomposition*. Examples of the successful application of the technique to Cartesian geometries were given in [18–20].

The 2D modelling of arbitrarily irregular boundaries on Cartesian grids is achieved, thanks to the original scheme presented by Barozzi et al. [23]. The technique involves a local modification of the computational stencil where boundary segments intersect the stencil arms.

The steady-state heat transfer predictions were carried out using the commercial finite-volume-based CFD code FLUENT (v. 6.2, © Fluent Inc.) in its time-independent option. A newly implemented third-order scheme for space discretization of momentum and energy equations was enforced [24], and the SIMPLE scheme [25] with second-order space discretizations was adopted to solve the pressure–velocity coupling. The use of the above high order schemes, combined with body-fitted meshes, is expected to guarantee high accuracy in the prediction of the local and averaged Nusselt numbers.

The iterative, point implicit, Gauss–Seidel linear equation solver implemented in FLUENT was used in conjunction with an algebraic multigrid (AMG) method, to solve for the temperature and the velocity components.

4. Development of the work

The geometry under consideration had not been previously characterized in terms of flow stability ranges. As a first issue, long-term flow behaviours were explored in terms of Ra_D, and d.

Four d-values were chosen, $d = 0.2$, 0.4, 0.6, and 0.8, with the first three corresponding to those already investigated in [13–15]. A 10×4 element matrix was set in the (Ra_D, d) plane, aimed to encompass the first stability

threshold for the four geometries: 10 values of Ra_D were selected for each value of d, covering the range of Ra_D from 10^2 up to 5×10^6 in a quasi-logarithmic sequence. DNS computations were performed over these 40 cases, and the long-term behaviour of the system was determined for each of them. Each run was initialized with a purely diffusive temperature field, as obtained by a preliminary zero-velocity simulation for the given Ra_D-value. In all the cases, the pressure and the velocity components were also initialized with fields generated numerically for $Ra_D = 10$.

The grids for the DNS solver were constructed using constant spacing $\xi = 0.01D$ in the central area, including the cylindrical source, so as to ensure accuracy in the approximation of the internal boundary. The same criterion was applied in the proximity of the cavity wall; a constant ratio coarsening was used to connect the central and the peripheral regions. A sample grid ($d = 0.4$) is shown in the upper part of Fig. 1.

A grid sensitivity analysis was carried out for the case $d = 0.2$, $Ra_D = 10^4$, where the flow regime turned out to be periodic. Spatial convergence was examined taking as the reference quantity the average non-dimensional wall heat flux on the right vertical side of the cavity. This is defined:

$$\varphi_{\mathrm{av}} = d \int_{\frac{1}{2d}}^{\frac{1}{2d}} \left. \frac{\partial T^*}{\partial x^*} \right|_{x^* = \frac{1}{2d}} \mathrm{d}z^*. \tag{22}$$

To check grid-dependency of unsteady solutions, three alternative indices were tried. These are: the dimensionless fundamental frequency of the system, ω; the oscillation amplitude, Φ; and the time-averaged heat flux over one oscillation period, $\bar{\varphi}_{\mathrm{av}}$. For all quantities, the relative error ε between each discrete solution, and the continuum value as predicted by Richardson extrapolation [26], was computed; results of the analysis are summarized in Table 1. The original (212×212) grid was halved once and twice ($k = 2$), while the maximum time-step size was inversely restricted.

It is pointed out that even the coarsest grid (53×53) correctly captured the periodic nature of the flow, although the solution was affected by severe quantitative errors. From Table 1, the oscillation amplitude, Φ, emerges as the most grid-sensitive of the three indices.

The small relative errors produced by the finest grid support the adoption of over-refined grids of that size, to ensure a satisfactory accuracy in the prediction of the asymptotic flows. The final grid sizes used for $d = 0.2$, 0.4, 0.6, and 0.8 were 212×212, 166×166, 144×144, 122×122 respectively.

Table 1
Sensitivity analysis for DNS grids

DNS grid $d = 0.2$ (no. of elements)	Relative error ε (%)		
	$\bar{\varphi}_{\mathrm{av}}$	ω	Φ
212×212	0.01	0.61	0.45
106×106	0.34	1.57	3.44
53×53	8.71	4.06	26.49

Table 2
Grid sizing for steady-state computations

d	Non-dimensional maximum grid spacing ξ/D	No. of elements
0.2	0.0540	5071
0.4	0.0383	2514
0.6	0.0227	2733
0.8	0.0070	9810

The long-term scenarios resulting from the numerical experiment were used to identify the subcritical ranges, i.e., the region of long-term steady-state flow conditions, for each of the four geometries. This formed the basis for the second part of the work, where the subcritical region was thoroughly explored.

Since the subcritical range is much more consistently defined in terms of Ra_H, rather than Ra_D, a new matrix of 22×4 points in the (Ra_H, d) plane was chosen to investigate the steady-state region. The CFD code FLUENT 6.2 was employed for steady-state predictions.

Special attention was again devoted to the mesh generation process, in order to produce high precision results and to achieve a satisfactory grid-independence. A grid sensitivity analysis was performed for $Ra_H = 2 \times 10^4$, the upper limit for steady-state, and the outermost d-values, $d = 0.2$ and $d = 0.8$. Richardson extrapolation [26] was again performed, φ_{av} being the reference quantity for spatial convergence. The average grid size, ξ, was chosen so as to guarantee a relative error on the reference quantity within 1% for $d = 0.2$ and $d = 0.8$. Those results were linearly interpolated to derive the appropriate average mesh size for the intermediate configurations ($d = 0.4$ and $d = 0.6$). The ξ-values obtained for each geometry were taken as the maximum cell dimension. A sample mesh for steady-state predictions is shown in the lower part of Fig. 1. The values of ξ and the number of grid elements used in final steady-state computations are reported in Table 2.

5. Results and discussion

5.1. Long-term flow regimes and subcritical region

Table 3 gives a qualitative view of the long-term scenarios resulting from DNS computations; different flow regimes match different greyscales in the table.

A rough distinction is made here between different steady-flow regimes, according to their thermal and flow patterns. In particular, the regimes where the temperature distribution does not deviate appreciably from the purely conductive one are defined pseudo-diffusive (PD); laminar symmetric (S) regimes are the ones where the thermal and flow fields are symmetric with respect to the central vertical axis ($x = 0$). Steady laminar non-symmetric (NS) thermal and flow fields sometimes appear. Time-dependent

Table 3
Characterization of asymptotic flow regimes from DNS computations

Ra_D	$d = .2$ $h = 2$	$d = .4$ $h = .15$	$d = .6$ $h = .333$	$d = .8$ $h = .125$
10^2	S	PD	PD	PD
$5 \cdot 10^2$	S	S	PD	PD
10^3	S	S	PD	PD
$5 \cdot 10^3$	S	S	S	PD
10^4	UP	S	S	PD
$5 \cdot 10^4$	UP	S	S	S
10^5	UC	S	S	S
$5 \cdot 10^5$	UC	UP	S	S
10^6	UC	UC	NS	S
$5 \cdot 10^6$	UC	UC	UC	S

PD = Pseudo-Diffusive; S = Steady Symmetric; NS = Steady Non-Symmetric; UP = Unsteady Periodic; UC = Unsteady Complex.

asymptotic flows are in turn designated unsteady periodic (UP), when a definite fundamental frequency is present in their power spectrum with or without its harmonics, or unsteady complex (UC), when more complex features are encountered.

Results indicate that various transitions occur at different Ra_D-values for different geometries, and, in particular, higher aspect ratios induce retarded transitions, in terms of Ra_D. The geometry is found not only to affect transition, but also the character of the supercritical flow regimes, and their stability ranges. This is particularly evident when comparing results for $d = 0.4$, and $d = 0.6$. In the former case a simple periodic regime is encountered after the first critical Ra_D-value, then followed by a more complex flow. For $d = 0.6$, on the contrary, a steady non-symmetric configuration precedes the transition to unsteady flow, and this is already complex in nature for $Ra_D = 5 \times 10^6$.

Overall, the results bear evidence of a progressive shift of the first supercritical Ra_D-value for increasing d; for example, the first transition occurs between 5×10^3 and 10^4, for $d = 0.2$, but falls above 5×10^6, for $d = 0.8$. Such a wide variability in the transitional regions in terms of Ra_D, suggest D might be not the most appropriate length scale for the problem at hand. For instance, L was preferred in previous studies [13–15]. The scaling effect of this quantity is however misleading, since, in fact, the leading parameter Ra_L is insensitive to the source diameter. On the other hand, D is the natural choice for isolated sources, but does not take into account the entity of confinement. The minimum gap between the confining walls and the source, H, is a more significant length: (i) it characterises regions of potentially maximum temperature gradients; (ii) the lateral gaps, where no stability constraint exists, are the initial flow promoters; (iii) the upper gap is a site of unstable thermal stratification.

The asymptotic flow-predictions for the 40 (Ra_D, d) couples were re-scaled in terms of (Ra_H, d) in Fig. 2. It is pointed out that regions associated with different long-term flow regimes become fairly more aligned on the Ra-axis, throughout the four d-values.

Results in Fig. 2 allow a common threshold for steady-state regimes to be coarsely defined, and, as a conservative estimate, the limit below which the asymptotic flow regime can be assumed to be stable steady-state is $Ra_H \cong 2 \times 10^4$, for $d \geqslant 0.2$.

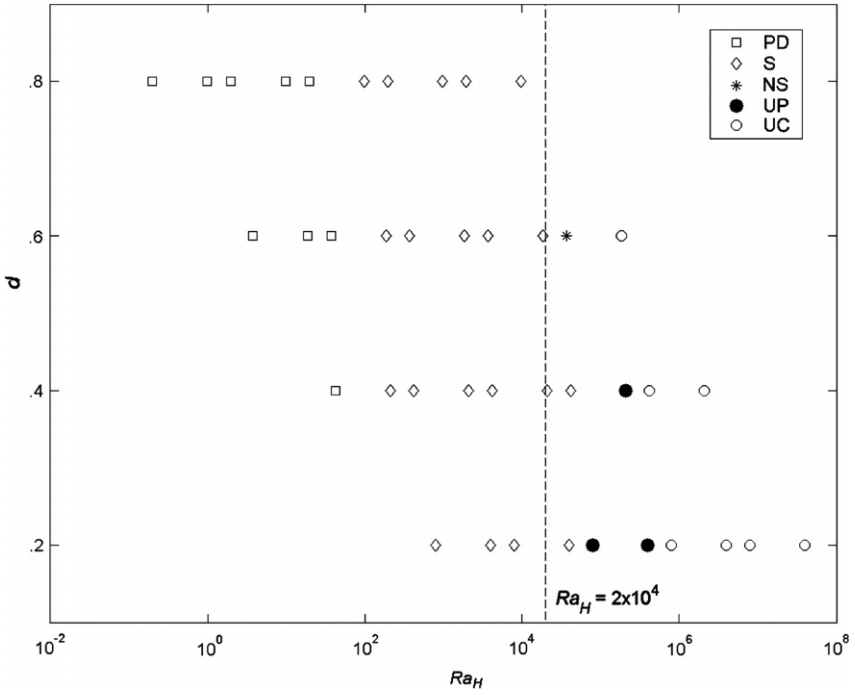

Fig. 2. Flow characterization from DNS on the (Ra_H, d) plane. PD = pseudo-diffusive; S = steady symmetric; NS = steady non-symmetric; UP = unsteady periodic; UC = unsteady complex.

5.2. Flow features

For all the d-values, with the exception of case $d = 0.2$, a purely diffusive thermal field and a very weak double-cell circulation correspond to the lowest Ra-values in Table 3. The flow is generated within the lateral gaps and propagates throughout the domain by viscous shear, as documented by the symmetry of the circulation cells towards the horizontal midplane. Fluid velocity however remains too low for the temperature distribution to be affected, and the thermal field does not deviate from a purely conductive one. At higher Rayleigh numbers, laminar steady-state convection prevails.

Fig. 3 demonstrates the influence of geometry on the general flow patterns and the thermal fields at steady-state. For each d-value, the case is shown corresponding to the maximum Ra_D-value for which a steady and symmetrical thermal-flow asset was predicted.

As reported by either Moukalled and Acharya [13] or Shu and Zhu [14], lower d ratios (Fig. 3a, and b) exhibit a common structure, characterized by the presence of a vertical thermal plume rising from the cylinder top and impacting the upper side of the cavity with, two big symmetrical and counter-rotating vortices dragging upwards fresh air from the bulk of fluid placed below the cylinder. The flow radically changes when increasing d up to 0.6 (Fig. 3c): in place of a single thermal plume, two smaller lateral plumes are now formed, while the fluid above the cylinder remains colder. The main circulations are pushed aside by the birth of two small counter-rotating secondary cells, which provide heat removal from the cylinder top. The above observations agree with previous findings in [13,14].

For $d = 0.8$, the flow field becomes even more complex (Fig. 3d). While the interchanges between the upper and the lower part of the cavity are strongly reduced, complex three-cell architectures appear in the upper part of the cavity. Besides the twin thermal plumes already observed for $d = 0.6$, the thermal boundary layer is perturbed in three more points: two small symmetrical temperature lumps are present just below the narrowing lateral gap, and a short plume reappears at the top of the cylinder. The former are due to a partial detachment of the main vortices, forced by the reduced space beside the cylinder at $\theta = 90°$. As a secondary effect, the circulation below the cylinder is strengthened. The latter effect is linked to the formation of a tertiary pair of cells above the cylinder, pushing aside the secondary vortices.

When Ra_D is increased up to values high enough to break the steady symmetric patterns, substantial differences in the behaviour of the four geometrical configurations appear.

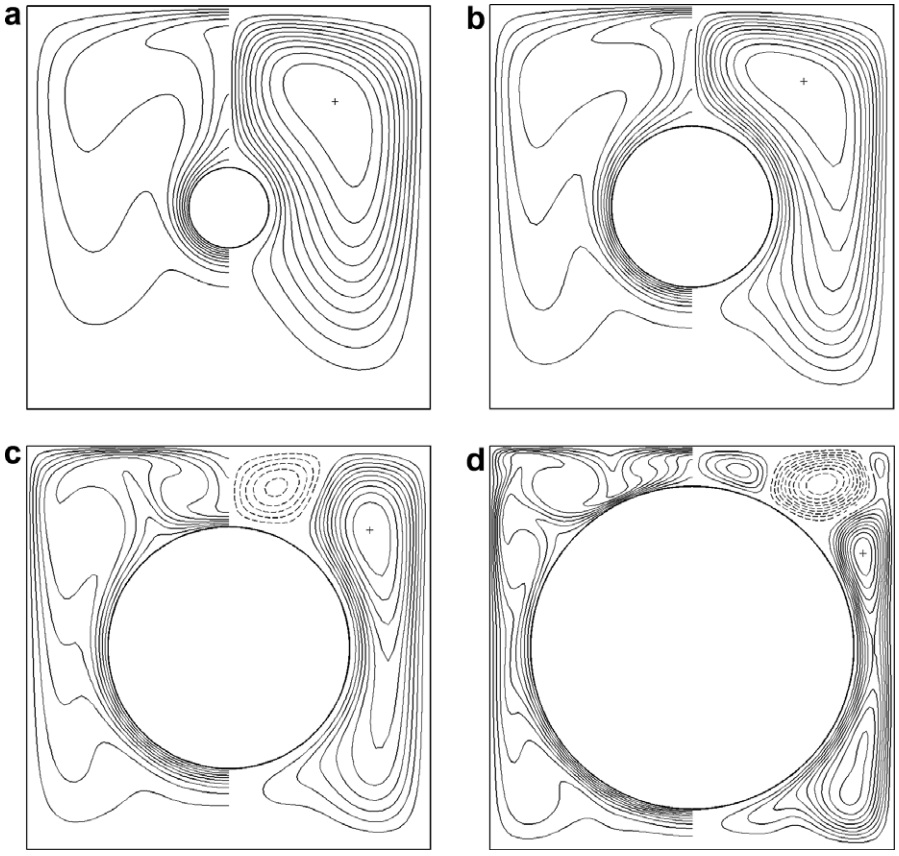

Fig. 3. Isotherms ($0.1 \leqslant T^* \leqslant 0.9$, left) and streamlines (right): (a) $d = 0.2$, $Ra_D = 5 \times 10^3$; (b) $d = 0.4$, $Ra_D = 10^5$; (c) $d = 0.6$, $Ra_D = 5 \times 10^5$; (d) $d = 0.8$, $Ra_D = 5 \times 10^6$. Continuous and dashed lines respectively indicate clockwise and counterclockwise circulation. (+) point of maximum for streamfunction.

For $d = 0.2$, a range of unsteady periodic flows is encountered. The power spectrum of the heat flux at the enclosure upper wall, for the UP case $Ra_D = 10^4$, exhibits a very neat peak at $\omega = 0.667$. According to Desrayaud and Lauriat [16], this behaviour indicates the occurrence of a Hopf bifurcation. The snapshot of the temperature field shown in Fig. 4, refers to the flow patterns predicted at $Ra_D = 10^5$. It should be pointed out that the central buoyant plume, always present in steady-state regimes for $d = 0.2$, still remains well defined, in spite of the more complex character of the flow.

The scenario remains similar for $d = 0.4$, with the onset of a periodic regime at a higher Ra_D-value.

Among the 10 solutions carried out for $d = 0.6$, transitional characteristics were only found for the two upper Ra_D-values. For $Ra_D = 10^6$, the long-term prediction is still steady-state, but non-symmetric, as shown in Fig. 5. The transient behaviour of this case was monitored by frame-by-frame displaying and time series analysis, leading to the conclusion that the non-symmetric pattern is formed by the progressive degeneration of a symmetric unstable configuration, through which the solution invariably passes. This symmetry-breaking pattern is typical of pitchfork bifurcations. Such an occurrence is not uncommon in confined buoyant flows [16,27].

For $Ra_D = 5 \times 10^6$, the circulation within the cavity becomes unsteady, and exhibits a complex periodicity. Fig. 6 reports time series for the average non-dimensional heat flux on the two vertical sides of the cavity: the two quantities are found to oscillate around different time-averaged values. This seems to indicate that this periodic flow originates from one of the branches of the above pitchfork bifurcation. In particular, the case shown in Fig. 6 falls on the same branch of the non-symmetric steady solution in Fig. 5. An asymptotic time-averaged solution is likely to lie upon it, as demonstrated by Desrayaud and Lauriat [16] for an enclosed line source. In that case a pitchfork branching was found to be followed by a subcritical Hopf bifurcation.

For none of the Rayleigh numbers examined at $d = 0.8$ the solution strayed from a symmetric steady-state configuration.

The issue of flow transition had not been discussed in previous works [13–15]. However, an estimate of the critical Ra-value can be inferred from Desrayaud and Lauriat [16], who detected a supercritical Hopf bifurcation at $Ra_L = 1.5\text{–}1.6 \times 10^6$, for a line heat source centred in a square cavity. For the smallest cylinder size considered here, $d = 0.2$, the first Ra-value associated with a periodic flow corresponds to $Ra_L = 1.25 \times 10^6$. Such a value compares very favourably with the stability threshold in [16], in view of the significant differences in the source size and the thermal boundary conditions at the enclosure walls.

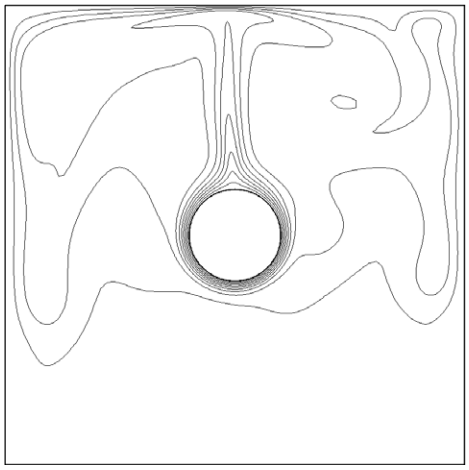

Fig. 4. Isotherms ($0.1 \leqslant T^* \leqslant 0.9$) for $d = 0.2$, $Ra_D = 10^5$.

5.3. Heat transfer results and correlation

Results are restricted to the subcritical region, characterized by the occurrence of a long-term steady-state regime.

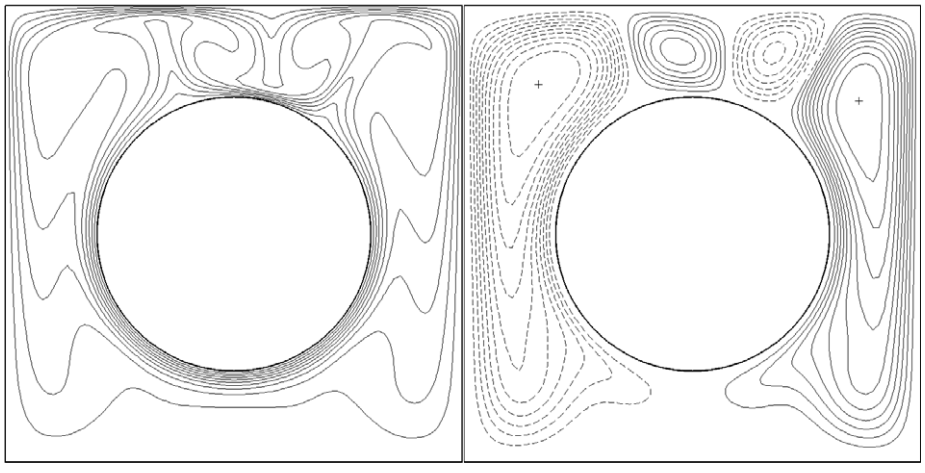

Fig. 5. Isotherms ($0.1 \leqslant T^* \leqslant 0.9$, left) and streamlines (right): $d = 0.6$, $Ra_D = 10^6$. Continuous and dashed lines respectively indicate clockwise and counterclockwise circulation. (+) points of maximum and minimum for streamfunction.

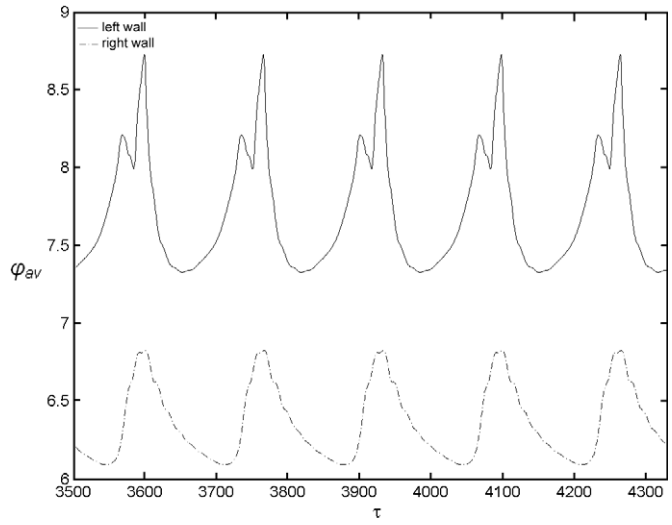

Fig. 6. Time histories of the average non-dimensional heat flux φ_{av} the left and right walls: $d = 0.6$, $Ra_D = 5 \times 10^6$.

Table 4 reports the 22×4 (Ra_H, d) matrix adopted for computations, and the related Nu_D- and Nu_H-values. The experiment covers the range of Ra_H from 10^{-9} to 2×10^4, therefore encompassing the pseudo-diffusive and the laminar regions.

Results in Table 4 confirm that pseudo-diffusive regimes are characterized by a constant value of the Nusselt number, which is attained asymptotically as Ra_H tends to zero; here this is labelled $Nu_{H,0}$.

Fig. 7 shows the distributions of the ratio $Nu_{H,\theta}/Nu_{H,\theta}$ along the cylinder contour, for selected Ra_H-values and d-ratios. The plots bring out the correspondence between the flow structures described in Section 5.2 and the resulting heat transfer modes. For the lower d-values (Fig. 7a and b) $Nu_{H,\theta}$ always exhibits a monotonically decreasing trend from the cylinder bottom ($\theta = 0$) to its top ($\theta = \pi$). This behaviour is coherent with Fig. 3a, and b, where the strong lateral vortices are seen to enhance convection in the lower part of the cylinder, while a progressive thickening of the boundary layer is observed for increasing θ, and one single stagnation point is present at $\theta = \pi$.

Over a comparable range of Ra_H, Cesini et al. [12] found similar trends in their experiments on a heating cylinder in an almost-square enclosure.

For either $d = 0.6$, and $d = 0.8$, the wall heat flux distribution becomes increasingly more irregular for increasing Ra_H, as a counterpart of the complexity the thermal and flow fields take on. Plots in Fig. 7c and d indicate that, even for the lowest Ra_H-value shown (2×10^4), the heat flux oscillates around the pseudo-diffusive value. For higher Ra_H-values, a profound dip and a very high peak appear in the upper part of the cylinder. For $d = 0.6$ the maximum always falls at $\theta = \pi$, while for $d = 0.8$, it progressively shifts backwards, down to 0.86π, for increasing Ra_H. As can be seen in Fig. 3c and d, minima in the $Nu_{H,\theta}/Nu_{H,\theta}$ plots match the presence of thermal plumes detaching from the cylinder surface, and maxima correspond to regions where fresh fluid is carried towards the wall by secondary or tertiary circulation cells.

The averaged values of the Nusselt number in Table 4 form the database used to derive a general heat transfer correlation covering the whole subcritical range. After

Table 4
Average Nusselt number values versus Ra_H, steady-state predictions

Ra_H	$Nu_D \mid Nu_H$			
	$d = 0.2$ $h = 2$	$d = 0.4$ $h = 0.75$	$d = 0.6$ $h = 0.333$	$d = 0.8$ $h = 0.125$
1×10^{-9}	1.1869|2.3737	2.0159|1.5120	3.4119|1.1373	6.7839|0.8480
1×10^{-7}	1.1869|2.3737	2.0159|1.5120	3.4119|1.1373	6.7839|0.8480
1×10^{-5}	1.1869|2.3737	2.0159|1.5120	3.4119|1.1373	6.7839|0.8480
1×10^{-3}	1.1869|2.3737	2.0159|1.5120	3.4119|1.1373	6.7839|0.8480
1×10^{-1}	1.1869|2.3737	2.0159|1.5120	3.4119|1.1373	6.7839|0.8480
1×10^{0}	1.1869|2.3737	2.0159|1.5120	3.4119|1.1373	6.7839|0.8480
1×10^{2}	1.1869|2.3738	2.0160|1.5120	3.4121|1.1374	6.7859|0.8482
5×10^{2}	1.1877|2.3755	2.0173|1.5129	3.4156|1.1385	6.8330|0.8541
1×10^{2}	1.1903|2.3807	2.0212|1.5159	3.4265|1.1422	6.9650|0.8706
2×10^{2}	1.2007|2.4014	2.0368|1.5276	3.4694|1.1565	7.2895|0.9112
3×10^{2}	1.2178|2.4357	2.0627|1.5470	3.5364|1.1788	7.5652|0.9457
4×10^{2}	1.2413|2.4827	2.0978|1.5733	3.6181|1.2060	7.7933|0.9742
1.2×10^{3}	1.5293|3.0587	2.5065|1.8799	4.2747|1.4249	9.2567|1.1571
2×10^{3}	1.7724|3.5449	2.8703|2.1527	4.9748|1.6583	10.5374|1.3172
2.85×10^{3}	1.9575|3.9151	3.1750|2.3812	5.5949|1.8650	11.5263|1.4408
5.3×10^{3}	2.2971|4.5943	3.7776|2.8332	6.7625|2.2542	13.5636|1.6955
7.75×10^{3}	2.5154|5.0309	4.1766|3.1325	7.5297|2.5099	14.9101|1.8638
1.02×10^{4}	2.6795|5.3591	4.4795|3.3597	8.1042|2.7014	16.0451|2.0056
1.265×10^{4}	2.8122|5.6243	4.7267|3.5450	8.5653|2.8551	16.9856|2.1232
1.51×10^{4}	2.9238|5.8475	4.9366|3.7024	8.9523|2.9841	17.7987|2.2248
1.755×10^{4}	3.0202|6.0404	5.1194|3.8395	9.2872|3.0957	18.5128|2.3141
2×10^{4}	3.1049|6.2099	5.2809|3.9607	9.5831|3.1944	19.1429|2.3929

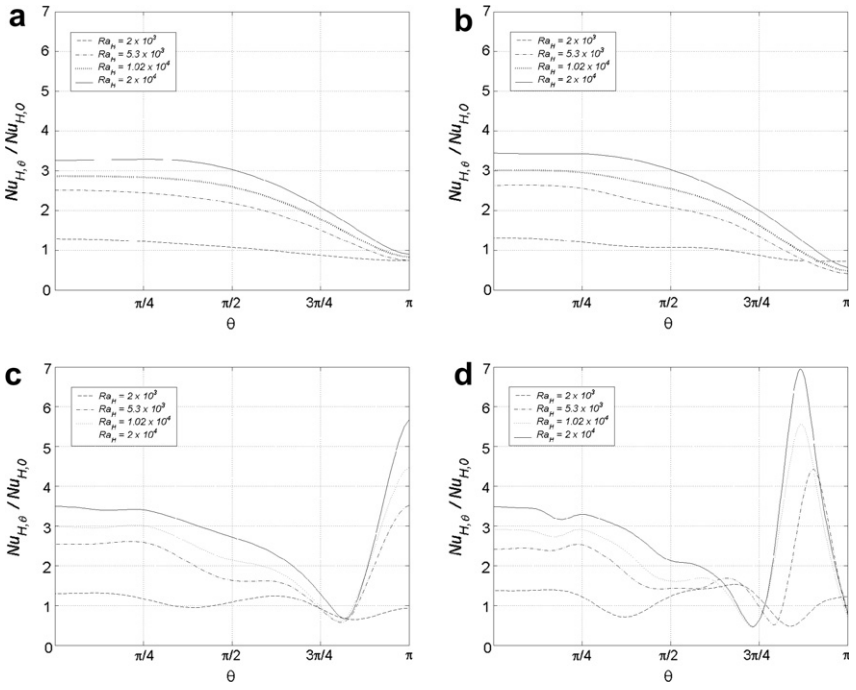

Fig. 7. Distributions of the local Nusselt number $Nu_{H\theta}$, along the cylinder surface for $Ra_H = 2 \times 10^3 - 2 \times 10^4$; (a) $d = 0.2$; (b) $d = 0.4$; (c) $d = 0.6$ and (d) $d = 0.8$. Data are normalized by pseudo-diffusive values $Nu_{H\,0}$, in Table 4.

trials, the variables to correlate were chosen to be Nu_H, Ra_H, and h. Note that $h = 2$, 0.75, 0.333, and 0.125 respectively correspond to $d = 0.2$, 0.4, 0.6, and 0.8.

Following the procedure outlined by Churchill and Usagi [28] and Churchill and Chu [9], asymptotic values for $Nu_H(Ra_H \to 0)$ and $Nu_H(Ra_H \to \infty)$ were correlated for each value of h, and the coefficients of the resulting equations expressed as a function of h.

The general correlation form [28] is:

$$Y = (1 + Z^n)^{-n}, \tag{23}$$

where Y and Z stand for:

$$Y = \frac{Nu_H(Ra_H, h)}{Nu_H(Ra_H \to 0, h)}, \tag{24}$$

$$Z = \frac{Nu_H(Ra_H \to \infty, h)}{Nu_H(Ra_H \to 0, h)}. \tag{25}$$

As already noted, constant $Nu_{H,0}$-values are obtained for $Ra_H \to 0$. Their power fitting as a function of h is:

$$Nu_H(Ra_H \to 0, h) = 0.54 + 1.178h^{0.637} \tag{26}$$

The seven highest Ra_H-values in Table 4 stood out as the cases where a steady convective regime is fully established. They were used to derive the asymptotic correlation for $Nu_H(Ra_H \to \infty)$. Those data were fitted by a power law equation for each of the four h-values:

$$Nu_H(Ra_H \to \infty) = aRa_H^b. \tag{27}$$

Values obtained for a and b are reported in Table 5. These were linearly related to h as follows:

Table 5
Constants in power-law Eq. (27) for each h-value

d	h	a	b
0.2	2	0.6653	0.2258
0.4	0.75	0.3305	0.251
0.6	0.333	0.2474	0.2586
0.8	0.125	0.18	0.2613

$$a(h) = 0.15 + 0.256h, \tag{28}$$

$$b(h) = 0.265 - 0.02h. \tag{29}$$

The dependence of b on h is weak, but was retained in order to improve the accuracy of the correlation.

Overall, the equation for $Nu_H(Ra_H \to \infty, h)$ turns out to be

$$Nu_H(Ra_H \to \infty, h) = (0.15 + 0.256h)Ra_H^{(0.265-0.02h)}. \tag{30}$$

The exponent n in Eq. (23) is given the integer value which minimizes the sum of the squared deviations between the original data and the predicted values. Here, $n = 14$ was found to be the best fitting value.

Substituting Eqs. (26) and (30) in Eq. (23) yields the following general correlation:

$$Nu_H(Ra_H, h) = \left\{\left(0.54 + 1.178h^{0.637}\right)^{14} + [(0.15 + 0.256h)Ra_H^{(0.265-0.02h)}]^{14}\right\}^{\frac{1}{14}}. \tag{31}$$

The ranges of validity of Eq. (31) are:

$$\begin{cases} Pr = 0.7, \\ 10^{-9} \leqslant Ra_H \leqslant 2 \times 10^4, \\ 0.125 \leqslant h \leqslant 2 \ (0.2 \leqslant d \leqslant 0.8). \end{cases} \tag{32}$$

Statistical analysis gives 0.994 for the R-square coefficient, with a maximum relative error of 7.2% for Eq. (31) towards the original database.

Eq. (31) is plotted in Fig. 8, using the coordinates Y, Z defined by Eqs. (24) and (25); two broken lines delimit the ±5% confidence level of the equation, and available literature data [13–15] are added.

In the literature, the only alternative to Eq. (31) for the geometry at hand is the correlation proposed by Moukalled and Acharya [13]:

$$Nu_D = 0.59 Ra_L^{0.23} \left(\frac{d}{2}\right)^{0.57}. \tag{33}$$

Eq. (33), properly re-scaled, is also plotted in Fig. 8 for the various h-values. It should pointed out that the predictions of Eq. (33) fall within the ±5% confidence range of Eq. (31) only for the intermediate h-values ($h = 0.75$ and 0.333), while results for $h = 0.125$, and $h = 2$ are underestimated. Furthermore, the exponent 0.23 in Eq. (33) matches the asymptotic trend given by Eq. (31) only for case $h = 2(d = 0.2)$.

A complete check of the predictive accuracy of Eq. (31) is reported in Table 6, where percentage deviations of the numerical results found in the literature are presented. All the data fall within a ±10% strip. Steady-state predictions in [13–15] which fall above the proposed stability threshold, $Ra_H \cong 2 \times 10^4$, have been starred in Table 6. It is interesting to remark that even those results are in good agreement with Eq. (31).

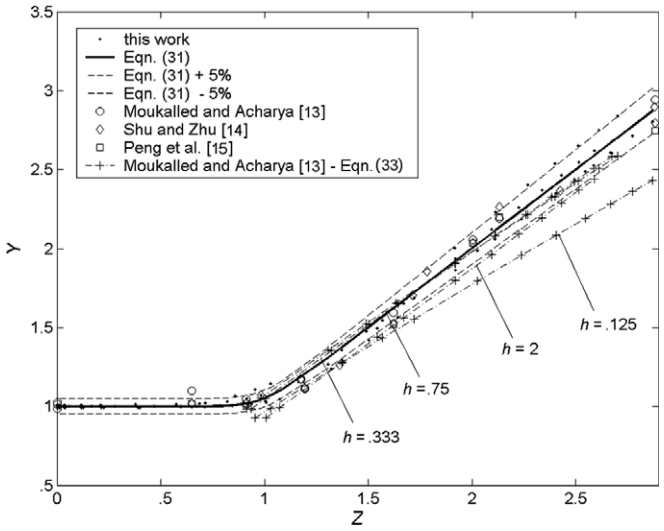

Fig. 8. Heat transfer correlation (31), as compared with available literature data. Coordinates Y and Z are defined in Eqs. (24) and (25).

Finally, the cases $Ra_L = 10^6$ and $d = 0.2$, 0.4, 0.6. in the literature [13–15], were re-calculated for direct compari-

Table 6
Deviations of available literature data from equation (31), and Nu_H predictions for selected Ra_L-values

d	h	Ra_L	Ra_D	Ra_H	ε % on Nu_H (Eq. (31))			Flow region
					Peng et al. [15]	Shu and Zhu [14]	Moukalled and Acharya [13]	
0.2	2	0	0	0	–	–	1.44	PD
0.2	2	1×10^4	8×10^1	6.4×10^2	7.05	7.05	7.45	S
0.2	2	5×10^4	4×10^2	3.2×10^2	–	0.82	–	S
0.2	2	1×10^5	8×10^2	6.4×10^3	−1.46	−1.46	−2.40	S
0.2	2	5×10^5	4×10^3	3.2×10^4	–	−0.64	–	S
0.2	2	1×10^6	8×10^3	6.4×10^4	4.96*	2.57*	2.62*	S/UP
0.2	2	1×10^7	8×10^4	6.4×10^5	–	–	2.59*	UP/UC
0.4	0.75	0	0	0	–	–	−2.35	PD
0.4	0.75	1×10^4	6.4×10^2	2.7×10^2	0.02	0.02	−2.79	S
0.4	0.75	5×10^4	3.2×10^2	1.35×10^3	–	7.50	–	S
0.4	0.75	1×10^5	6.4×10^3	2.7×10^3	6.27	5.88	1.62	S
0.4	0.75	5×10^5	3.2×10^4	1.35×10^4	–	2.47	–	S
0.4	0.75	1×10^6	6.4×10^4	2.7×10^4	4.70*	3.07*	−2.09*	S
0.4	0.75	1×10^7	6.4×10^5	2.7×10^5	–	–	3.29*	UP/UC
0.6	0.333	0	0	0	–	–	−1.27	PD
0.6	0.333	1×10^4	2.16×10^3	8×10^1	−1.65	−1.83	−9.87	PD/S
0.6	0.333	5×10^4	1.08×10^4	4×10^2	–	−2.77	–	S
0.6	0.333	1×10^5	2.16×10^4	8×10^2	1.27	1.11	1.08	S
0.6	0.333	5×10^5	1.08×10^5	4×10^3	–	−4.01	–	S
0.6	0.333	1×10^6	2.16×10^5	8×10^3	−3.06	−6.16	−2.80	S
0.6	0.333	1×10^7	2.16×10^6	8×10^4	–	–	6.35*	NS/UC

d	h	Ra_L	Ra_D	Ra_H	Nu_H [22]	Nu_H [21]	Nu_H [20]	Nu_H (this work)
0.2	2	1×10^6	8×10^3	6.4×10^4	7.589	7.779	7.776	7.769
0.4	0.75	1×10^6	6.4×10^4	2.7×10^4	4.178	4.249	4.476	4.243
0.6	0.333	1×10^6	2.16×10^5	8×10^3	2.472	2.546	2.466	2.532

* Predictions in [13–15] falling above the proposed stability threshold.

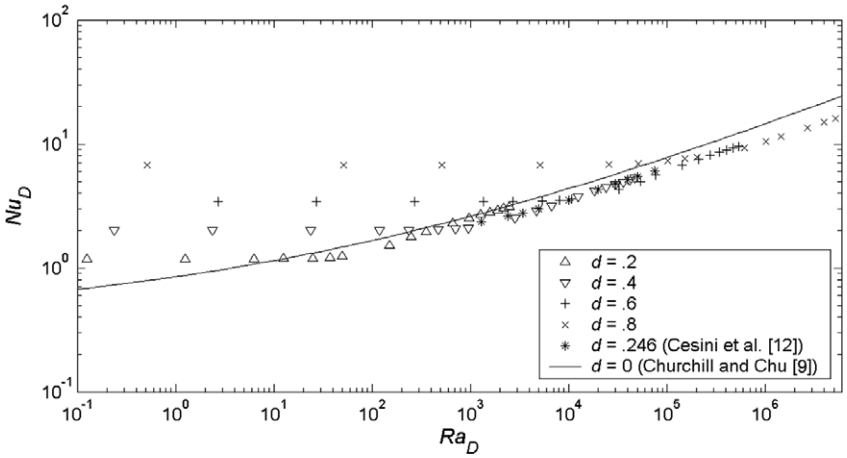

Fig. 9. Nu_D–Ra_D plot of the present prediction, as compared with Churchill and Chu [9] and Cesini et al. [12].

son. Results are presented in the lower part of Table 6 in terms of Nu_H. The agreement with present predictions is satisfactory and, in particular, an excellent correspondence emerges with the results by Shu and Zhu [14]. Apart for some of the data from Moukalled and Acharya [13], the deviations from Eq. (31) listed in Table 6 are indicative of the accuracy of the correlation itself, which should be safely stated to be better than $\pm 10\%$ over the whole range.

In most practical situations, the diameter of the heating source, D, and the leading temperature difference, ΔT, are the design parameters, while the shape and size of the encapsulation is to be chosen. Data in Table 4, scaled back to the (Ra_D, d) format, have been plotted in Fig. 9. They show that, as long as pseudo-diffusive regimes prevail, Nu_D increases with d, for a given Ra_D-Value. However, the more room available for fluid circulation, implied by low-d sizing, promotes heat transfer for increasing Ra_D. Churchill's and Chu [9] equation for the free-stream cylinder, also plotted in Fig. 9, fits coherently with the above observations, showing that the free-stream cylinder ($d \to 0$) is the most efficient solution for $Ra_D \to \infty$. However, the unbounded option penalises heat transfer in the low-Ra_D range, in comparison to the enclosed geometries, and, for $d = 0.8$ this holds true up to $Ra_D \cong 4 \times 10^4$.

A final comparison can be made with the results of Cesini et al. [12], for an isothermal horizontal cylinder in a rectangular cavity having isothermal sides and a conductive ceiling. One of the three cavities considered was almost square, with $d = 0.246$. Nu_D-values were inserted in Fig. 9 for that geometry. It can be seen that they fall between the present predictions for $d = 0.2$ and $d = 0.4$, suggesting that a change in the cavity boundary conditions does not substantially affect the heat transfer rate.

6. Concluding remarks

Natural convection heat transfer from a horizontal cylinder centred in an air filled cavity of square cross-section, was investigated numerically. Four values of the diameter-to-side ratio were considered, $d = 0.2$, 0.4, 0.6, 0.8. The last geometry had never been investigated previously.

A wide range of Rayleigh numbers was explored, also encompassing the stability limit for long-term steady-regimes. Substantial differences were observed in the flow and thermal fields, depending on the aspect ratio and the Rayleigh number, in the regions of either asymptotically-steady or time-dependent flows. Pseudo-diffusive, steady-symmetric, periodic, and more complex time-dependent flow-regimes were detected. A steady non-symmetric solution was also encountered for $d = 0.6$.

The range of stable laminar flows was roughly identified for each geometry, and the critical value of the Rayleigh number based on D, Ra_D, was found to vary within one order of magnitude when passing from one d-value to the next. It was possible to reconcile this wide variability by reassembling the transitional data in terms of Ra_H, the Rayleigh number based on the gap-width between the top of the cylinder and the upper cavity wall. The stability threshold of steady-state solutions was conservatively fixed at $Ra_H = 2 \times 10^4$, same for all the four geometries. Even if rough, this estimate is the only one available for this class of problems, for the time being.

The regions of long-term steady solutions were thoroughly explored using the commercial CFD package FLUENT, while enforcing the steady-state formulation and high-order spatial discretizations.

A correlating equation for the average Nusselt number on the cylinder, as a function on both the Rayleigh number and the diameter-to-side ratio, was derived, covering the whole steady-state region. Extensive comparison with the available literature data allowed to ascribe the correlation an accuracy better than $\pm 10\%$.

Acknowledgements

This research was fully supported by "Ministero dell'Istruzione, Università e Ricerca" (MIUR) of Italy, under the scheme "Projects of National Interest 2005", Grant No. 2005094817.

References

[1] G.F. Hewitt (Ed.), Handbook of Heat Exchanger Design, Begell House, New York, 1992, pp. 2.5.7.20–2.5.7.23.

[2] A. Bejan, Convection Heat Transfer, first ed., Wiley, New York, 1984, pp. 159–201.

[3] F.P. Incropera, D.P. DeWitt, Fundamentals of Heat and Mass Transfer, fifth ed., Wiley, New York, 2002, pp. 534–572.

[4] S. Ostrach, Natural convection heat transfer in cavities and cells, in: U. Grigull, E. Hahne, K. Stephan, J. Straub (Eds.), Proceedings of the Seventh International Heat Transfer Conference, Hemisphere, Washington DC, 1982, pp. 365–379.

[5] S. Ostrach, Natural convection in enclosures, J. Heat Transfer 110 (1988) 1175–1190.

[6] B. Gebhart, Y. Jaluria, R.L. Mahajan, B. Sammakia, Buoyancy-Induced Flows and Transport, Hemisphere, Washington D.C., 1988, pp. 725–814.

[7] R.O. Warrington Jr., R.E. Powe, The transfer of heat by natural convection between bodies and their enclosures, Int. J. Heat Mass Transfer 28 (2) (1985) 319–330.

[8] W.H. McAdams, Heat Transmission, third ed., McGraw-Hill, New York, 1954.

[9] S.W. Churchill, H.S. Chu, Correlation equations for laminar and turbulent free convection from a horizontal cylinder, Int. J. Heat Mass Transfer 18 (1974) 1049–1053.

[10] V.T. Morgan, The overall convective heat transfer from smooth circular cylinders, in: T.F. Irvine Jr., J.P. Hartnett (Eds.), Advances in Heat Transfer, vol. 11, Academic Press, New York, 1975.

[11] N.K. Ghaddar, Natural convection heat transfer between a uniformly heated cylindrical element and its rectangular enclosure, Int. J. Heat Mass Transfer 35 (10) (1992) 2327–2334.

[12] G. Cesini, M. Paroncini, G. Cortella, M. Manzan, Natural convection from a horizontal cylinder in a rectangular cavity, Int. J. Heat Mass Transfer 42 (10) (1999) 1801–1811.

[13] F. Moukalled, S. Acharya, Natural convection in the annulus between concentric horizontal circular and square cylinders, J. Thermophys. Heat Transfer 10 (3) (1996) 524–531.

[14] C. Shu, Y.D. Zhu, Efficient computation of natural convection in a concentric annulus between an outer square cylinder and an inner circular cylinder, Int. J. Numer. Methods Fluids 38 (2002) 429–445.

[15] Y. Peng, Y.T. Chew, C. Shu, Numerical simulation of natural convection in a concentric annulus between a square outer cylinder and a circular inner cylinder using the Taylor-series expansion and least-squares-based lattice Boltzmann method, Phys. Rev. E 67 (2003), 026701–1–6.

[16] G. Desrayaud, G. Lauriat, Unsteady confined buoyant plumes, J. Fluid Mech. 252 (1993) 617–646.

[17] V. Deschamps, G. Desrayaud, Modeling a horizontal heat-flux cylinder as a line source, J. Thermophys. Heat Transfer 8 (1) (1994) 84–91.

[18] M.A. Corticelli, G.S. Barozzi, Numerical study of time-dependent buoyancy-induced cavity flows, in: E.W.P. Hahane, W. Heidemann, K. Spindler (Eds.), Proc. of the 3rd European Thermal Sciences Conf., vol. 1, Edizioni ETS, Pisa, 2000, pp. 387–392.

[19] G.S. Barozzi, M.A. Corticelli, Natural convection in cavities containing internal sources, Heat Mass Transfer 36 (2000) 473–480.

[20] G.S. Barozzi, M.A. Corticelli, Numerical simulation of time-dependent buoyant flows in a cavity containing an internal heat source, in: Proc. of the 6th UK National Conf. on Heat Transfer, Edinburgh, UK, IMechE Conf. Transact, Professional Engineering Publishings Ltd., London, 1999, pp. 69–74.

[21] D.D. Gray, A. Giorgini, The validity of the Boussinesq approximation for liquids and gases, Int. J. Heat Mass Transfer 19 (1976) 545–551.

[22] P.M. Gresho, On the theory of semi-implicit projection methods for viscous incompressible flow and its implementation via finite element method that also introduces a nearly consistent mass matrix. Part 1: theory, Int. J. Numer. Methods Fluids 11 (1990) 578–620.

[23] G.S. Barozzi, C. Bussi, M.A. Corticelli, A fast Cartesian scheme for unsteady heat diffusion on irregular domains, Numer. Heat Transfer B – Fundamentals 46 (2004) 56–77.

[24] Fluent User's Guide – Version 6.2, Fluent Inc., Canterra Resource Park, Lebanon, NH, 2003.

[25] S.V. Patankar, Numerical Heat Transfer and Fluid Flow, first ed., Hemisphere, Washington DC, 1980, pp. 126–135.

[26] P.J. Roache, Computational Fluid Dynamics, first ed., Hermosa, Socorro, NM, 1972, pp. 177–178.

[27] G.A. Holtzman, R.W. Hill, K.S. Ball, Laminar natural convection in isosceles triangular enclosures heated from below and symmetrically cooled from above, J. Heat Transfer 122 (3) (2000) 485–491.

[28] S.W. Churchill, R. Usagi, A general expression for the correlation of rates of transfer and other phenomena, AIChE J. 18 (6) (1972) 1121–1128.